Modelling of Cracks with Frictional Contact Based on Peridynamics

Wei Lu[1], Selda Oterkus[2*], Erkan Oterkus[2], Dagang Zhang[1]

[1] *College of Shipbuilding Engineering, Harbin Engineering University, Harbin, China*
[2] *PeriDynamics Research Centre, Department of Naval Architecture, Ocean and Marine Engineering, University of Strathclyde, Glasgow, UK*

Abstract

In this study, a two-dimensional peridynamic contact model is proposed to model the propagation of frictional crack within the peridynamic framework. Compared with traditional numerical method in peridynamics, no additional algorithm is needed for implementing the contact constraint. The geometry of the crack can be easily described by the rupture of bond without any extra enrichment functions. In this model, the contact force is regarded as a short-range force and only related to the stretch of the virtual bond between the disconnected material points. The sliding of the plates under compression and the plate with a pre-existing crack under compressive loading have been simulated to validate the accuracy of the peridynamic contact model. By introducing the bond skew failure criterion, the propagation of the frictional crack is modelled as well. The growth path of the crack matches the numerical result obtained based on the phase field method. Therefore, peridynamics can be demonstrated as an effective numerical tool to solve the frictional contact problem.

Keywords: Peridynamics; Frictional contact; Crack propagation; Fracture

1. Introduction

For the fracture of brittle material, its final failure strongly depends on the initial discontinuities, such as the pre-existing cracks and voids. In the past decades, various numerical simulations have been done on fracture of polycrystal materials, such as rocks [1], metals [2,3], ceramics [4,5] and so on. When modelling the fracture of polycrystal material, due to the grain boundary sliding which occurs under the compression, the influence of the frictional contact along the crack cannot be neglected. Besides, the frictional crack is also widely implemented in many branches of civil and mechanical engineering areas. For instance, in forming process, the relative displacement between the tool and work piece generates friction force which affects many aspects of the process including the density distribution, final shape, residual stresses and crack initiation. [6,7] Thus, understanding the frictional contact behavior plays a significant role in predicting the material response in many applications. Various algorithms for the numerical solutions of the contact problem are presented in the literature [8,9].

In continuum mechanics, when modelling friction, the displacement constraints should be satisfied including the normal constraint to prevent the penetration of the domains, and the tangential displacement to control the contact boundary sliding. Commonly, two constraint methods are utilized in the finite element solution to enforce the surface contact constraint; the Lagrange multiplier method and the penalty function method. In the Lagrange multiplier approach, the Lagrange multiplier vector is introduced into the equation of motion as an unknown variable and the no-penetration condition is imposed simultaneously [10,11]. In the penalty approach, the normal contact force incorporating an additional penalty factor depends on the penetration between the contact surface [12]. Traditional finite element method faces significant challenges in modelling the propagation of frictional crack since the repeated remeshing and predicting the growth direction of crack in advance are needed to ensure the discontinuous displacement field lies on the boundary of the element. Therefore, by enriching a standard

*Corresponding author: selda.oterkus@strath.ac.uk

displacement-based approximation with additional discontinuous interpolation functions through the partition of unity method, the extended finite element (X-FEM) is proposed [13-15] to allow the entire crack being described independently of mesh within the finite element framework. No mesh updating of the domain is required in modelling the crack propagation. As forerunners, Dolbow et al. [16] applied X-FEM method with the adaption of iterative scheme employed in Large Time Increment (LATIN) method to model the frictional contact on arbitrary evolving interfaces. To solve the nonlinear boundary problem, the formulation is divided into linear global and nonlinear local parts. The penalty approach is utilized by Khoei and Nikbakht [17] with X-FEM, in which the enrichment is in accordance with Heaviside step function, to simulate the frictional sliding. However, the implementation of the Lagrangian or penalty method, employing the constraints on embedded interfaces, may result in oscillations in the interfacial fields and less convergence in local error norms, showing as numerical instability in discretization [18-19]. Based on the Uzawa-type augmented Lagrangian multiplier approach, a contact formulation within X-FEM framework is depicted by Hirmand et al. [20] for modelling the frictional discontinuity. The Lagrange multipliers and penalty method are combined in this paper to attain high accuracy satisfaction of the constraint condition and reduce the ill condition of the governing equation. To resolve the nonlinear equations, an active set strategy is imposed combined with the Newton–Raphson iterative solution. Coon et al. [21] used X-FEM with Nitsche method applying on the boundary conditions to solve the earthquake rupture. Nevertheless, when the geometry of the interface is much more complicated, it will be difficult to impose the constraint conditions on the interface and the process of enrichment may cause large number of unknown variables in the algebraic system. Thus, Fei and Choo [22] introduced the phase-field method for modelling the cracks with frictional contact. The contact behaviors and constraints are included by calculating the stress tensor of the interface. Generally, the finite difference method or finite element method is used to solve the equation which gives rise to large computation amount and limits the development of three-dimensional modelling. For all these reasons, peridynamic contact model is utilized for solving the frictional crack problems in this study. Peridynamics is a non-local particle method introduced by Silling [23] to handle the discontinuity issue. There has been significant progress in peridynamic research since its introduction [24-39]. In the peridynamic governing equation, the partial derivatives of displacements are replaced by the integral form. Recently, in rock mechanics and engineering field, peridynamics has been widely used to simulate the fracture behaviors of rock and rock-like materials under different mechanical and multi-physical boundary conditions [40]. Non-ordinary state based peridynamics was applied to model the crack propagation and coalescence in rock-like materials with pre-existing flaws under uniaxial compressive loads or biaxial compressive loads [41]. In this model, the maximum tensile stress criterion and the Mohr-Coulomb criterion were incorporated to distinguish the tension and shear failure. The same NOSB PD model was also implemented to simulate the crack propagation and coalescence in Brazilian disks [42]. By introducing the rotation of the conjugated bond under shear deformation, the bond based peridynamics was improved as conjugated bond-based peridynamics which overcomes the limitation of Poisson's ratio in the regular PD model [43-45]. Besides the pair-wise force along the direction of bond, the tangential force perpendicular to the bond direction was considered as well. The failure criterion was updated with addition of the critical bond shear energy density. Thus, both Mode I and Mode II/III fracture can be described. The novel numerical conjugated bond-based peridynamic model has been developed into both two-dimensional and three-dimensional models. This novel bond-based peridynamic model captures the crack initiation, propagation and coalescence well in the simulation of rock-like materials under compressive and shear loadings. To study pressurized and fluid driven fracture problems in fissured porous rocks, a new coupled

hydromechanical bond-based peridynamic model was proposed by Zhou et al. [46]. Based on the Biot's theory, the equation of motion of bond-based peridynamics was reformulated. The fracture criterion is updated in the hydromechanical peridynamic model to simulate the failure caused by high fluid pressure. Both pressurized-driven fracture and fluid-driven fracture cases have been calculated, verifying the accuracy of the hydromechanical peridynamic model. For the friction field, Kamensky et al. [47] introduced a friction model based on the state-based peridynamics. Frictional collision of two blocks and the impact between a tough spherical ball and a brittle block are simulated. Zhang and Qiao [48] investigated the frictional contact for axisymmetric problem to model the pull-out tests.

In this study, frictional contact model is proposed within the peridynamic framework. No extra algorithm involving the contact constraint is needed. The normal contact pressure depends on the stretch of the bond. The friction force can be obtained from the Coulomb's law. Several benchmark problems have been simulated to validate the peridynamic frictional contact model. Finally, by using the peridynamic model, the propagation of a frictional crack is investigated.

2.Brief Review of Peridynamics

As an efficient implementation to solve the discontinuity problem, peridynamics is introduced by Silling [23] as a meshfree method with the reformulation of integral equation. Interactions between material points occur within finite distance, called horizon here. Peridynamic theory is classified into two main approaches, bond-based peridynamics and state-based peridynamics. In bond-based peridynamic theory, the interaction force between particles only depends on the stretch of the single bond between two material points and is not influenced by the other bonds inside the horizon. The bond-based method is commonly used in various numerical simulations of the material fracture. Nevertheless, the limitation of effective Poisson's ratio which is 1/3 in two-dimensional models narrows its application. Thus, as an improvement, the state-based peridynamics is also proposed by Silling [49] to overcome the limitations of bond-based peridynamics. In this model, the force between the particles is not only influenced by the stretch of a single bond, but also the stretch of all bonds inside the horizons of interacting material points. In peridynamics, the equation of motion for an infinitesimal volume dV at position $\mathbf{x}$ at time t is written as [49],

$$\rho(\mathbf{x})\ddot{\mathbf{u}}(\mathbf{x},t) = \int_{H_{\mathbf{x}}} (\underline{\mathbf{T}}[\mathbf{x},t]\langle \mathbf{x}'-\mathbf{x}\rangle - \underline{\mathbf{T}}[\mathbf{x}',t]\langle \mathbf{x}-\mathbf{x}'\rangle) dV_{\mathbf{x}'} + \mathbf{b}(\mathbf{x},t) \tag{1}$$

in which ρ represents the mass density in the reference configuration, $\mathbf{u}$ is the displacement vector field, $H_{\mathbf{x}}$ represents the horizon of point $\mathbf{x}$ with the radius of δ, $\mathbf{b}$ is the body force density field and $\underline{\mathbf{T}}$ is the force vector state which is aligned with the deformation state and can be expressed as

$$\underline{\mathbf{T}}[\mathbf{x},t]\langle \mathbf{x}'-\mathbf{x}\rangle = \underline{t}\langle \mathbf{x}'-\mathbf{x}\rangle \frac{\underline{\mathbf{Y}}\langle \mathbf{x}'-\mathbf{x}\rangle}{\left\|\underline{\mathbf{Y}}\langle \mathbf{x}'-\mathbf{x}\rangle\right\|} \tag{2}$$

where $\underline{t}$ is the scalar part of the force vector state and $\underline{\mathbf{Y}}$ represents the deformation state, mapping the original bond vector into the deformed bond vector (seen in Figure 1), denoted by $\underline{\mathbf{Y}}\langle \mathbf{x}'-\mathbf{x}\rangle = \underline{\mathbf{X}}\langle \mathbf{x}'-\mathbf{x}\rangle + \underline{\mathbf{U}}\langle \mathbf{x}'-\mathbf{x}\rangle$. $\underline{\mathbf{X}}$ defines the relative position of the bond in the initial configuration, depicted as, $\underline{\mathbf{X}}\langle \mathbf{x}'-\mathbf{x}\rangle = \mathbf{x}'-\mathbf{x}$, whereas the displacement state is defined as $\underline{\mathbf{U}}\langle \mathbf{x}'-\mathbf{x}\rangle = \mathbf{u}(\mathbf{x}',t) - \mathbf{u}(\mathbf{x},t)$.

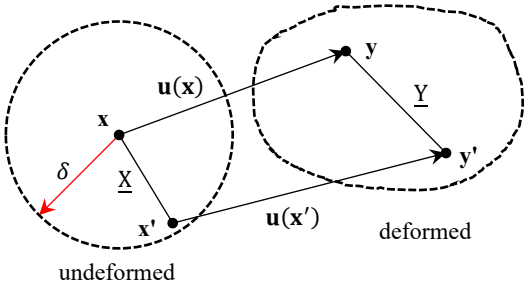

Fig. 1 Schematic for the deformation of the bond

By making analogy with the three-dimensional model, for the plane stress problem, a nonlocal scalar dilatation function is defined first [50] with the value equivalent to the volume dilatation.

$$\theta = \frac{2(2v-1)}{(v-1)} + \frac{\underline{\omega x} \cdot \underline{e}}{m} \tag{3}$$

in which v is the Poisson's ratio of the material and $\underline{\omega}$ is influence function valued between 0 and 1, depending on the length of bond. Here, $\underline{x}$ is the scalar value of the position state $\underline{\mathbf{X}}$ and $\underline{e}$ represents the scalar extension state, denoted by $\underline{e} = \|\underline{\mathbf{Y}}\| - \|\underline{\mathbf{X}}\|$, indicating the length of bond elongation. m is called weighted volume which is defined as [49],

$$m = \underline{\omega x} \cdot \underline{x} = \int_{H_{\mathbf{x}}} \underline{\omega} |\mathbf{x}' - \mathbf{x}|^2 \, dV_{\mathbf{x}'} \tag{4}$$

According to Silling and Lehoucq [51], assuming a peridynamic material model for a linear isotropic elastic solid, the peridynamic strain energy density function W is defined as,

$$W(\underline{\mathrm{Y}}) = \frac{k'\theta^2}{2} + \frac{\alpha}{2}(\underline{\omega e^d}) \cdot \underline{e^d} \tag{5}$$

where k' and α are parameters need to be deduced. $\underline{e^d}$ represents the deviatoric part of the extension state $\underline{e}$, which can be calculated as

$$\underline{e^d} = \underline{e} - \frac{\theta \underline{x}}{3} \tag{6}$$

In continuum mechanics, for the linear elastic model, the classical strain energy density Ω in plane stress is written as,

$$\Omega = \left[\frac{k}{2} + \mu\left(\frac{(v+1)}{3(2v-1)}\right)^2\right]\left(\frac{dV}{V}\right)^2 + \mu \sum\nolimits_{i,j=1,2} \varepsilon_{ij}^d \, \varepsilon_{ij}^d \tag{7}$$

where k and μ are bulk and shear moduli of the material, respectively, dV/V represents the volume dilatation and ε_{ij}^d is the ij component of the deviatoric part for the strain tensor.

By equalizing the peridynamic strain energy density function with the strain energy of a material point in the continuum mechanics [44], the parameters k' and α can be obtained as

$$\alpha = \frac{8\mu}{m}, \qquad k' = k + \frac{\mu}{9}\frac{(v+1)^2}{(2v-1)^2} \tag{8}$$

To attain the scalar force vector state, the Fréchet derivative of equation 5 with respect to the extension state is calculated as

$$\Delta W = k'\theta(\nabla_{\underline{e}}\theta) \cdot \Delta\underline{e} + \alpha(\underline{\omega e^d}) \cdot \Delta\underline{e^d} = \left[\left(k'\theta - \frac{\alpha}{3}(\underline{\omega e^d}) \cdot \underline{x}\right)\nabla_{\underline{e}}\theta + \alpha\underline{\omega e^d}\right] \cdot \Delta\underline{e} \tag{9}$$

Thus, the scalar force vector state is written as

$$\underline{t} = \frac{2(2\nu-1)}{(\nu-1)}\left(k'\theta - \frac{\alpha}{3}\left(\underline{\omega e}^d\right)\cdot \underline{x}\right)\frac{\underline{\omega x}}{m} + \alpha \underline{\omega e}^d \tag{10}$$

Here, $\underline{t}$ is the magnitude of the force vector state $\underline{\mathbf{T}}$. Substituting the force vector state into the governing equation, the acceleration of the material point can be obtained.

3.Peridynamic contact model

In this study, a peridynamic contact model is defined to describe the sliding along the contact surface. Due to the shrinkage of the undeformed body, the contact between the disconnected surface and the boundary sliding cannot be neglected. Contact of the material points includes the particles which belong to different bodies during the simulation and ones become disconnected due to the bond rupture. When two disconnected material points are getting close enough, a kind of repelling force will be generated to prevent the different material points from sharing the same position. This repelling force is commonly calculated as a short-range force [52]. Thus, when the distance between the two disconnected material points is smaller than a critical distance δ_c, a contact interaction occurs. A contact model should be built between them, as shown in Figure 2. In this study, the critical distance is defined as the radius of the contact area H_c to justify whether there is a contact pairwise force between two material points in the current configuration. In Figure 2, S represents the contact interface of two bodies, resulting from the pre-existing crack or the newly formed crack. $\mathbf{y}$ and $\mathbf{y}'$ are the position of material points in the current configuration corresponding to the initial material points $\mathbf{x}$ and $\mathbf{x}'$, respectively. Besides, the normal contact force state $\underline{\mathbf{T}_n}$ and friction contact force state $\underline{\mathbf{T}_f}$ are proposed as the external forces to depict contact model. Therefore, taking the contact model into consideration, the peridynamic equation of motion can be reformulated as

$$\begin{aligned}\rho(\mathbf{x})\ddot{\mathbf{u}}(\mathbf{x},t) = &\int_H \left(\underline{\mathbf{T}}[\mathbf{x},t]\langle \mathbf{x}''-\mathbf{x}\rangle - \underline{\mathbf{T}}[\mathbf{x}'',t]\langle \mathbf{x}-\mathbf{x}''\rangle\right)dV_{\mathbf{x}''} + \mathbf{b}(\mathbf{x},t)\\ &+\int_{H_c}\Big(\underline{\mathbf{T}_n}[\mathbf{x},t]\langle \mathbf{x}'-\mathbf{x}\rangle - \underline{\mathbf{T}_n}[\mathbf{x}',t]\langle \mathbf{x}-\mathbf{x}'\rangle + \underline{\mathbf{T}_f}[\mathbf{x},t]\langle \mathbf{x}'-\mathbf{x}\rangle\\ &-\underline{\mathbf{T}_f}[\mathbf{x}',t]\langle \mathbf{x}-\mathbf{x}'\rangle\Big)\,dV_{\mathbf{x}'}\end{aligned} \tag{11}$$

in which the normal contact force state is perpendicular of the contact interface and the friction contact force is parallel to the sliding interface, opposite to the relative sliding displacement.

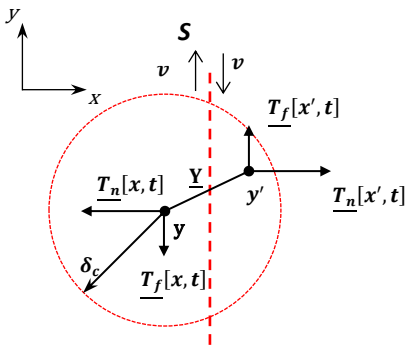

Fig. 2 The sketch of the peridynamic contact model

In equation 11, $\int_H \left(\underline{\mathbf{T}}[\mathbf{x},t]\langle \mathbf{x}''-\mathbf{x}\rangle - \underline{\mathbf{T}}[\mathbf{x}'',t]\langle \mathbf{x}-\mathbf{x}''\rangle\right) dV_{\mathbf{x}''}$ is the peridynamic force. $\mathbf{b}(\mathbf{x},t)$ represents the external body force and $\int_{H_c} \left(\underline{\mathbf{T}_n}[\mathbf{x},t]\langle \mathbf{x}'-\mathbf{x}\rangle - \underline{\mathbf{T}_n}[\mathbf{x}',t]\langle \mathbf{x}-\mathbf{x}'\rangle + \underline{\mathbf{T}_f}[\mathbf{x},t]\langle \mathbf{x}'-\mathbf{x}\rangle - \underline{\mathbf{T}_f}[\mathbf{x}',t]\langle \mathbf{x}-\mathbf{x}'\rangle\right) dV_{\mathbf{x}'}$ is the contact force acting on the material point **x.** Referring [53], the decomposition of the acceleration of material point x is shown in figure 3.

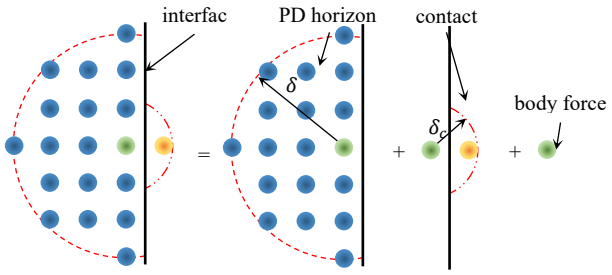

Fig. 3 The decomposition of the acceleration of material point **x**

Assuming the contact interface is along the y-axis of the local coordinate, the normal contact force and friction force can be respectively written as,

$$\underline{\mathbf{T}_n}\langle \mathbf{x}'-\mathbf{x}\rangle = -\underline{t_n}\langle \mathbf{x}'-\mathbf{x}\rangle \mathrm{sgn}\left(\underline{\mathbf{Y}}\langle \mathbf{x}'-\mathbf{x}\rangle \cdot \mathbf{e}_x\right)\mathbf{e}_x \tag{12}$$

$$\underline{\mathbf{T}_f}\langle \mathbf{x}'-\mathbf{x}\rangle = \underline{t_f}\langle \mathbf{x}'-\mathbf{x}\rangle \mathrm{sgn}\left[\frac{\partial}{\partial t}\left(\left(\underline{\mathbf{Y}}\langle \mathbf{x}'-\mathbf{x}\rangle - \underline{\mathbf{X}}\langle \mathbf{x}'-\mathbf{x}\rangle\right)\cdot \mathbf{e}_y\right)\right]\mathbf{e}_y \tag{13}$$

where $\underline{t_n}$ and $\underline{t_f}$ are the scalar of the contact force states. $\mathbf{e}_x$ and $\mathbf{e}_y$ represent the unit vector along the x-axis and y-axis directions, respectively. According to the Coulomb's law, the relationship between the normal contact force and the friction contact force can be established as

$$\underline{t_f}\langle \mathbf{x}'-\mathbf{x}\rangle = f_c \underline{t_n}\langle \mathbf{x}'-\mathbf{x}\rangle \tag{14}$$

in which f_c stands for the friction coefficient of the interface.

Compared to the contact model used in the two-dimensional axisymmetric pull-out numerical model by Zhang and Qiao [48], similar ideas have been implemented in this study for the ordinary two-dimensional plate. Under the hypothesis of the small displacement, the normal contact force state $\underline{t_n}$ is defined to restore the normal contact pressure p_c. It can be seen that the unit of the normal contact pressure state is Newton per square meter (N/m^2), while the unit of the normal contact force is Newton per sixth power of meter (N/m^6). The relationship between them is same as that of energy release rate G_c (J/m^2) and critical bond energy density w_c (J/m^6) [54], shown in equation 15 as

$$w_c\langle \mathbf{x}'-\mathbf{x}\rangle = \frac{3G_c}{2\delta^3 t_h} \tag{15}$$

in which t_h is the thickness of the plate.

Thus, by substituting the energy release rate and the critical bond energy density, the normal contact force state can be calculated as

$$\underline{t_n}\langle \mathbf{x}'-\mathbf{x}\rangle = \begin{cases} \dfrac{3p_c}{2\delta^3 t_h} & \text{if } \left|\underline{\mathbf{Y}}\langle \mathbf{x}'-\mathbf{x}\rangle\right| < \delta_c \\ 0 & \text{otherwise} \end{cases} \tag{16}$$

When the bond is ruptured, only contact force is considered between material points **x** and $\mathbf{x}'$, as the peridynamic force vanishes.

Referring to equation of pairwise force in the bond-based peridynamics, the normal contact pressure p_c can be evaluated proportional to the stretch of the virtual bond along the normal force direction,

$$p_c = E_c \left(\frac{\left| \underline{\mathbf{X}}\langle \xi \rangle \cdot \mathbf{e}_x \right| - \left| \underline{\mathbf{Y}}\langle \xi \rangle \cdot \mathbf{e}_x \right|}{\left| \underline{\mathbf{X}}\langle \xi \rangle \cdot \mathbf{e}_x \right|} \right) \tag{16}$$

Here, E_c is called the contact stiffness which can be evaluated in the 2D PD contact model as [55],

$$\frac{1}{E_c} = \frac{1 - v_1^2}{E_1} + \frac{1 - v_2^2}{E_2} \tag{17}$$

in which E_1 and E_2 are the elastic moduli of the two contact bodies on both sides of the interface.

To reduce the computation cost, we define a pre-contact area near the crack and the area of potential damage. For instance, as shown in Figure 4, the pre-contact areas are set along the boundary of plates. The width of the area is defined as twice of critical contact distance here ($L_c = 2\delta_c$) to ensure all the contact pair can be included in it. Since the contact interaction only exists in the rupture bond, we link the detection of contact with the failure coefficient, as shown in Figure 5. Under the assumption of small deformation, the corresponding contact material point can be considered inside the horizon centered by current referred particle. Therefore, when the failure coefficient equals to 0, which means the bond is broken, the distance between the two material points in the current configuration will be calculated. If the distance is shorter than the critical contact distance, there is contact interaction between two particles.

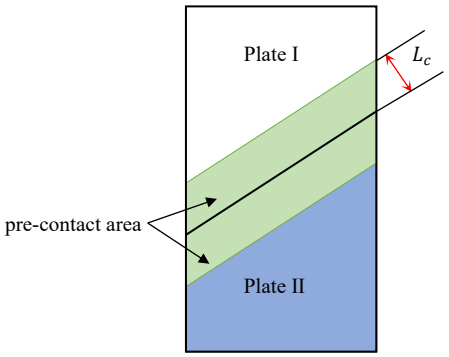

Fig.4 The schematic of pre-contact area

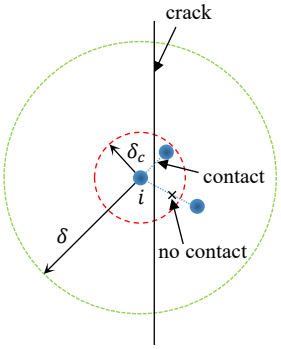

Fig.5 The schematic of detection of contact

4.Numerical Results

In this section, several static numerical cases have been analyzed by using the peridynamic contact model described above. The numerical results will be compared with the results obtained from FEM to verify the accuracy of the peridynamic contact model. Finally, the propagation of the frictional crack will be calculated in the peridynamic framework.

4.1 The sliding of the plate under compression with vertical contact surface

In this case, two thin plates with the length L of 60mm and the width D of 32mm are interacting with each other under compression state. Both of the plates are considered behaving as linear elastic material and both have the same material properties, of which the elastic modulus E is 60GPa and the Poisson's ratio v is 0.20. The thickness of the plate h is 2mm. For the boundary loading condition, uniformly distributed horizontal displacement $d_0 = 0.8$mm is applied at the right boundary of the right plate to generate the compressive state of the plate. While vertical displacement $d_1 = 0.8$mm is added at the top boundary of the left plate to pull out the plate. Because of the shrinkage of the plate, there will be friction between the two plates if the friction coefficient of the interface is not equal to zero. To transfer

the external loading displacements to the internal material points inside the plate, three fictious layers of particles are added at the top edge of the left plate and the right edge of the right plate. All the three virtual layers are subjected to loading displacement. In the numerical model, each plate is uniformly divided into 80 material points in horizontal direction and 150 material points in vertical direction, respectively, with the distance of $\Delta x = 0.4$mm between the particles. The radius of the horizon is defined as $\delta = 3\Delta x$, while the contact radius for searching the contact material points is $\delta_c = \Delta x$. Three fictitious layers of particles are added at the left boundary of the left plate by setting the horizontal displacement to zero to constrain the model. The same fictitious layers are applied at the bottom edge of the right plate as well, limiting the vertical displacement of the particles to zero to provide sufficient constrain for the calculation. Since the interaction process is regarded as quasi-static, the adaptive dynamic relaxation method (ADR) is used in the numerical simulation. Totally 10000 time steps are calculated to reach convergence. In this section, two friction coefficients are implemented in the simulation to show the effect of friction force.

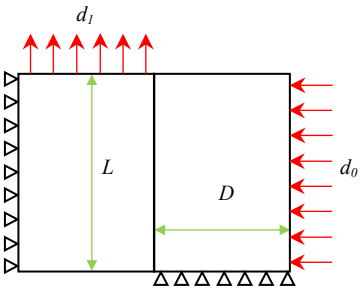

Fig. 6 The geometry sketch of the plates in contact

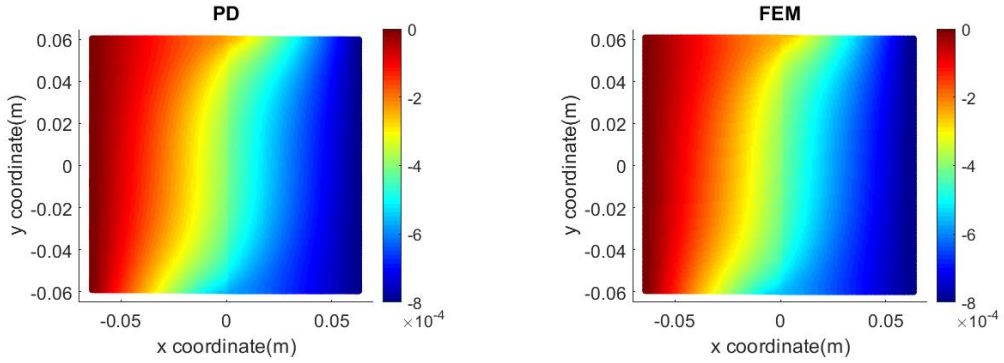

(a) The horizontal displacement of the plates in contact

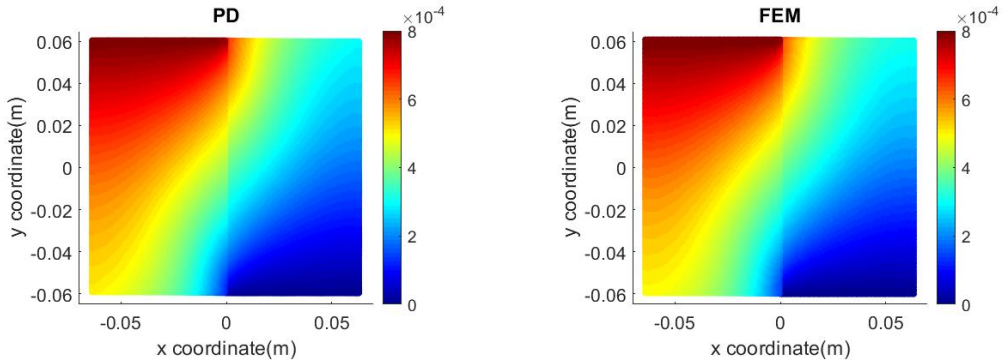

(b) The vertical displacement of the plates in contact

Fig. 7 The comparison of the displacements of the plates between the peridynamics and FEM (f_c =0.8)

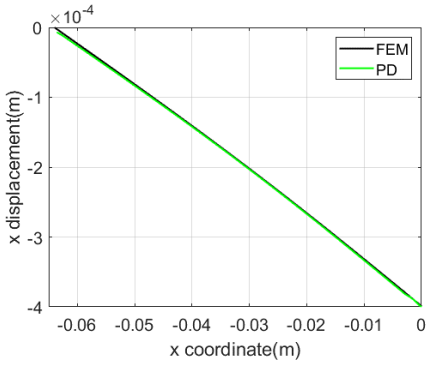

(a) The left plate

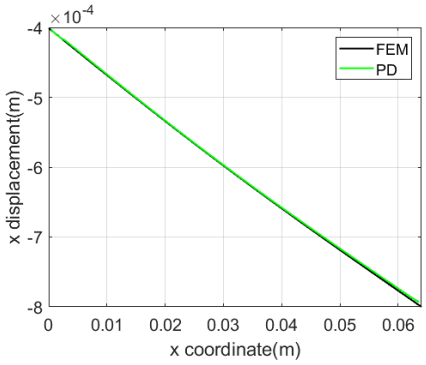

(b) The right plate

Fig. 8 The comparison of the horizontal displacement of along the central x axis between FEM and peridynamics (f_c =0.8)

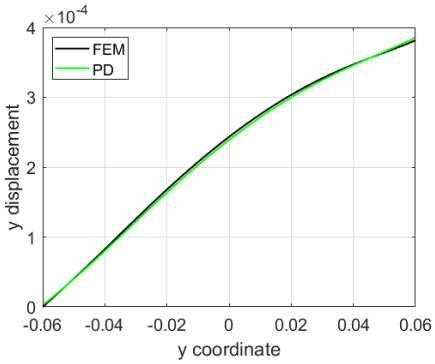

Fig. 9 The comparison of the vertical displacement along the vertical line (x=0.032) of the right plate between FEM and peridynamics (f_c =0.8)

When the coefficient f_c is equal to 0.8, as shown in Figures 7, 8 and 9, it can be clearly seen that the peridynamic numerical results show very good agreement with the FEM results obtained from ANSYS, a commercially available finite element software. Small difference only occurs in the vertical displacement field at the boundary of the plate due to the lack of intact horizon.

For the friction coefficient equals to 0.01, the peridynamic and FEM results of the sliding of the plate under compression are shown in Figures 10, 11, 12. From these figures, we can see that the displacement results of the peridynamics match well with the results obtained from FEM. For the material points near the boundary, there is some error in the vertical displacement field, as shown in Figure 12. When compared with the high value friction coefficient case, it can be seen that under same loading condition, when the contact surface is rougher, the peridynamic contact model shows higher accuracy.

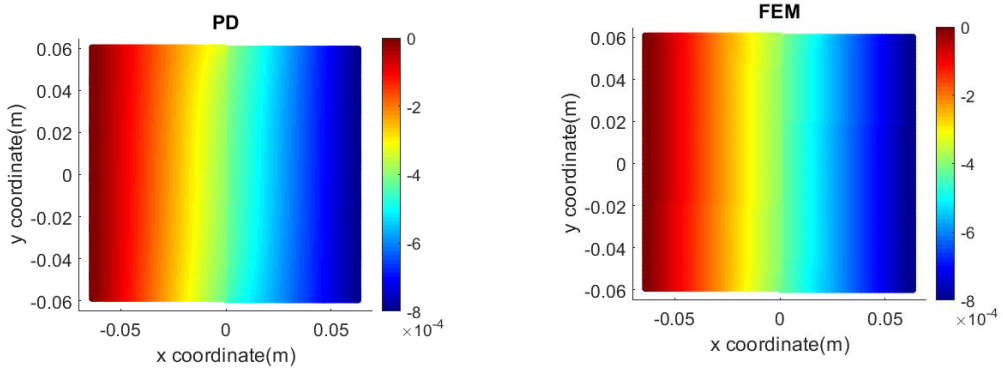

(a) The horizontal displacement of the plates in contact

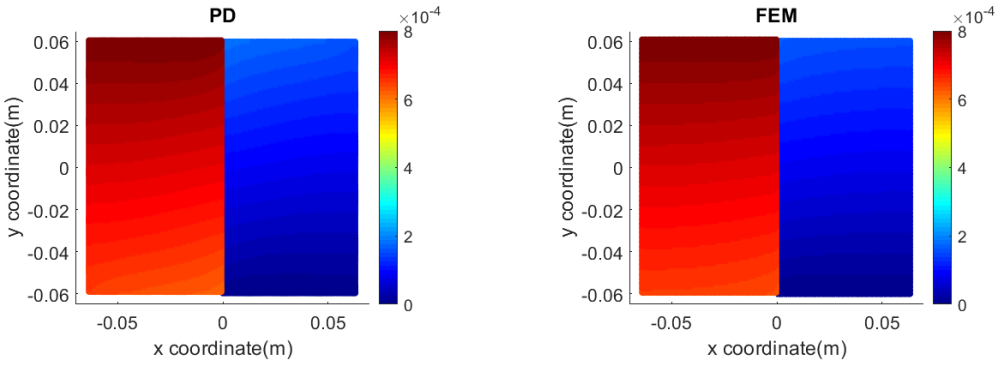

(b) The vertical displacement of the plates in contact

Fig. 10 The comparison of the displacement of the plate between the peridynamics and FEM (f_c =0.01)

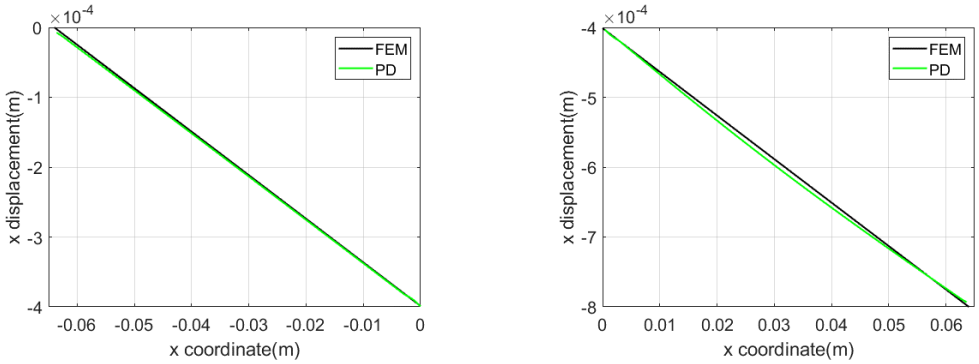

(a) The left plate (b) The right plate

Fig. 11 The comparison of the horizontal displacement along the central x axis between FEM and peridynamics (f_c =0.01)

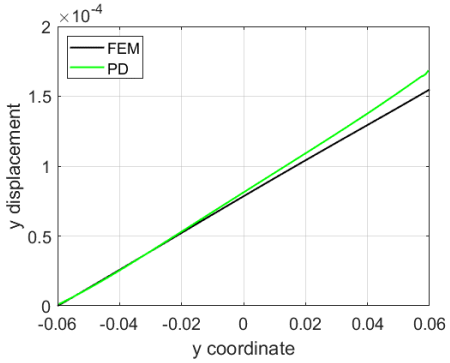

Fig. 12 The comparison of the vertical displacement along the vertical line (x=0.032) of the right plate between FEM and peridynamics (f_c =0.01)

When the friction coefficient equals to 0.8, different critical contact distances have been investigated. As shown in figure 13 and figure 14, the displacement results show convergence when the critical contact distance values are between 0.8 to 1.0 times of the distance between particles. When the critical distance equals to the space between the material points, the horizontal and vertical displacements match the FEM results best.

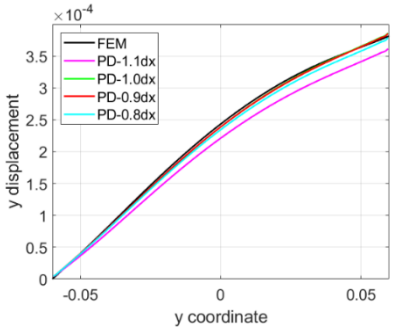

Fig. 13 The comparison of the vertical displacement along the vertical line (x=0.032) of the right plate with different critical contact distances

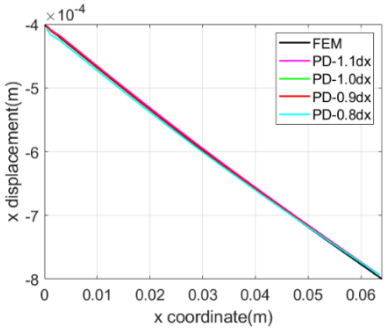

Fig. 14 The comparison of the horizontal displacement of along the central x axis of the right plate with different critical contact distances

4.2 The sliding of the plate under compression with inclined contact surface

In this case, the two thin plates have a length of l_0=1.0 × 10^{-3}m. The height of the shorter edge l_1 is set as 0.2 × 10^{-3}m, while the height of the longer edge l_2 is 1.0 × 10^{-3}m. The angle of the inclined contact surface is 45 degrees. Both plates are considered as linear elastic material, and both have the same material properties, of which the elastic modulus *E* is 10GPa and the Poisson's ratio υ is 0.20. The thickness of the plate *t* is 0.02mm. As the boundary loading condition, uniformly distributed horizontal displacement $d_0 = 0.5 \times 10^{-6}$ m is applied at the top boundary of the top plate to generate the compressive state of the plate, as shown in Figure 15. The loading displacement is imposed inside the fictious boundary region, which is composed of three virtual layers of particles added at the top edge of the top plate. Fictious layers of material points are also added at the bottom edge of the plate with the vertical displacement setting as zero to support efficient constraint. Horizontal constraint is applied on the shorter boundary of plate with additional three fictious layers of particles. The plates are discretized with 100 particles along the horizontal direction and 120 particles along the vertical direction, respectively. The contact radius here is defined as Δx=1.0 × 10^{-5}m, same as the spacing between the material points. The radius of horizon δ is equal to $3\Delta x = 3.0 \times 10^{-5}$m. In total 20000 time steps have been calculated to reach convergence.

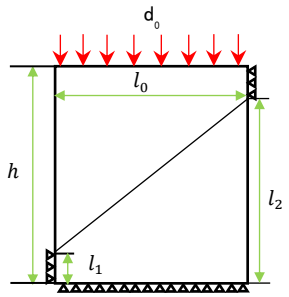

Fig. 15 The geometry sketch of the plates in contact with inclined contact surface

Both frictionless and friction case have been simulated. The comparison of the displacement field between the peridynamics and FEM is depicted in Figures 16 and 17, which clearly shows very good agreement. In the frictionless case, only normal contact force is considered. Compared with the friction case, the displacement field of frictionless one indicates higher accuracy. While for the case with the

friction coefficient of 0.8, there is some error in the horizontal displacement field near the sharp angle of the plate. From equation 13, it can be seen that the calculation of the friction force is related to the velocity of the particle. Therefore, in the static problem, the algorithm will bring some error, but the accuracy of the result is still acceptable.

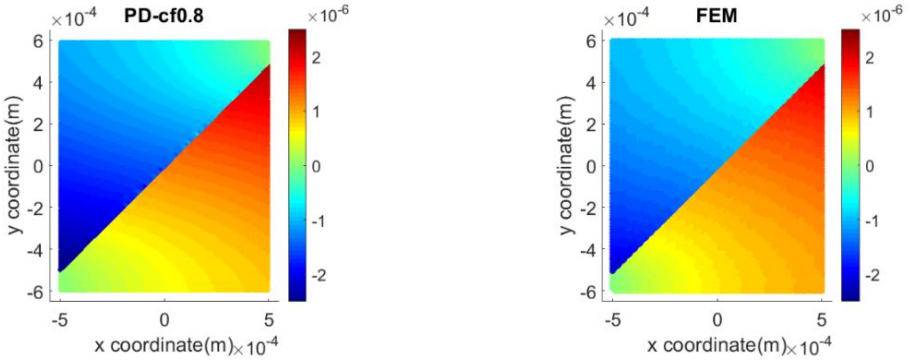

(a) The comparison of the horizontal displacement with the friction coefficient equal to 0.8

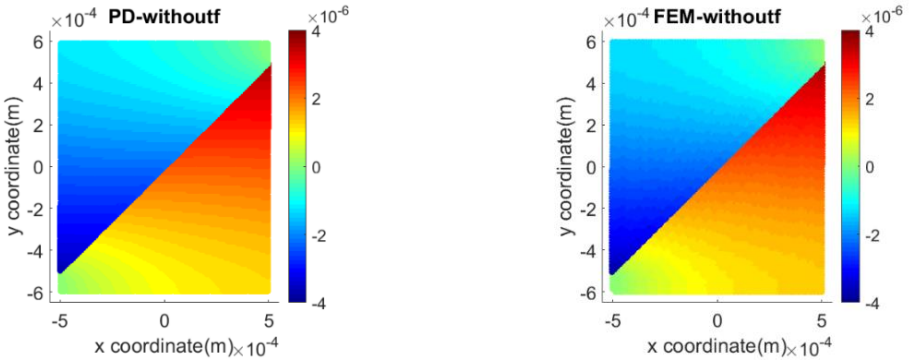

(b) The comparison of the horizontal displacement without friction

Fig. 16 The comparison of the horizontal displacement between PD and FEM

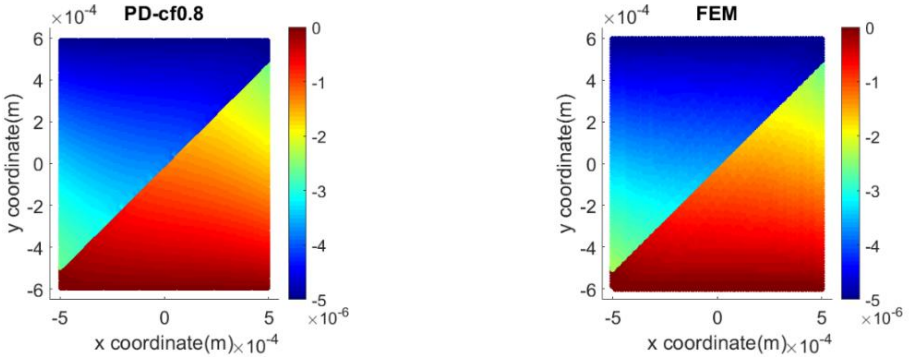

(a) The comparison of the vertical displacement with the friction coefficient equal to 0.8

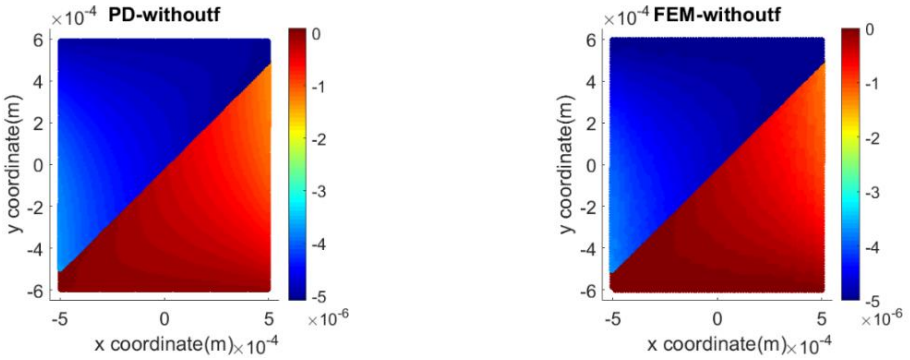

(b) The comparison of the vertical displacement without friction

Fig. 17 The comparison of the vertical displacement between PD and FEM

4.3 The plate under compression with a pre-existing crack inside

In this section, an initial crack is added inside the plate to investigate the influence of friction for the fracture. However, to simplify the problem, the propagation of the crack is not considered in this case. Here, the plate has a width of 1m, and a length of 1m. It is uniformly distributed into 100 particles along the vertical and horizontal directions, with a total of 10000 particles inside the solution domain. The radius of horizon δ is defined as 3.0×10^{-2}m, 3 times of the spacing between material points. A pre-existing crack is set at the center of the plate, with the angle of 45 degrees to the positive x direction. The tips of the crack are located at the coordinates of (-0.2, -0.2) and (0.2, 0.2) respectively, as shown in Figure 18. By breaking the bonds crossing the connecting line between (-0.2, -0.2) and (0.2, 0.2), the initial crack is inserted in the plate. Three fictious layers of material points are added at the bottom boundary of the plate to constrain the plate. Both the horizontal and vertical displacements of the fictious material points are set as 0. Uniform vertical displacement $d = 9\text{mm}$ is applied at the top boundary of the plate to generate deformation. To transfer the loading displacement to the internal plate, three virtual layers of particles are added as fictious boundary region at the top edge of the plate. The vertical displacement of the particles in this fictious boundary region is set as $d = 9\text{mm}$, while the horizontal displacement is constrained as 0. To ensure the stability of the numerical simulation, the adaptive dynamic relaxation is utilized. The contact radius δ_c is equal to Δx here.

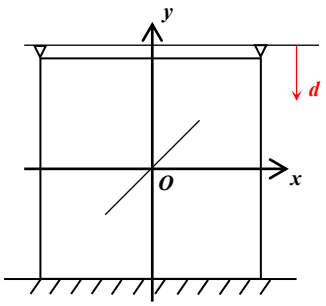

Fig. 18 The geometry sketch of the plate under compression with an initial crack inside

To study the effect of the contact model, three numerical cases have been considered; the case without contact, the case without friction, and the case with the friction coefficient of 0.8. From Figures 19, 20 and 21, it can be seen that the peridynamic results match well with the FEM results in all three cases. The comparison between Figures 19 and 20 shows that the normal contact force has an obvious influence on the horizontal displacement field. The normal contact force repels the particles getting close with each other, avoiding the penetration of the material points along the crack. Nevertheless, there is no much difference between Figures 20 and 21, which indicates less effect of friction force. Since the relative displacement along the crack direction is not obvious, the friction force is much smaller in comparison with the normal contact force, resulting in the less influence of friction force being insignificant in the displacement field.

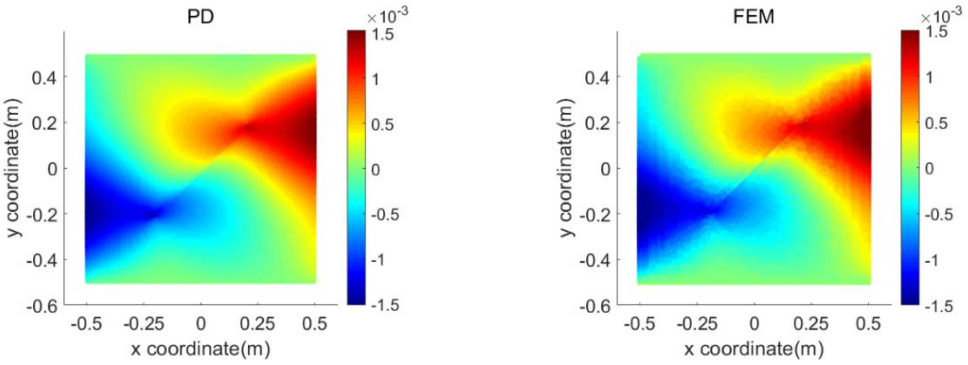

(a) The horizontal displacement field of the plate with initial crack inside

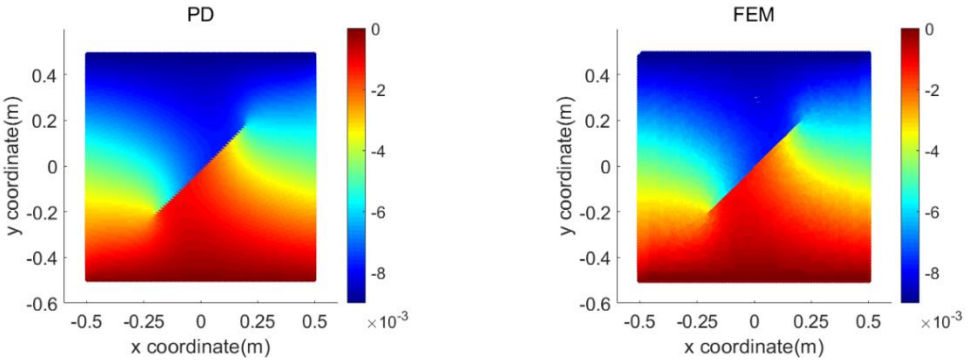

(b) The vertical displacement field of the plate with initial crack inside

Fig. 19 The comparison of the displacement field between PD and FEM without contact

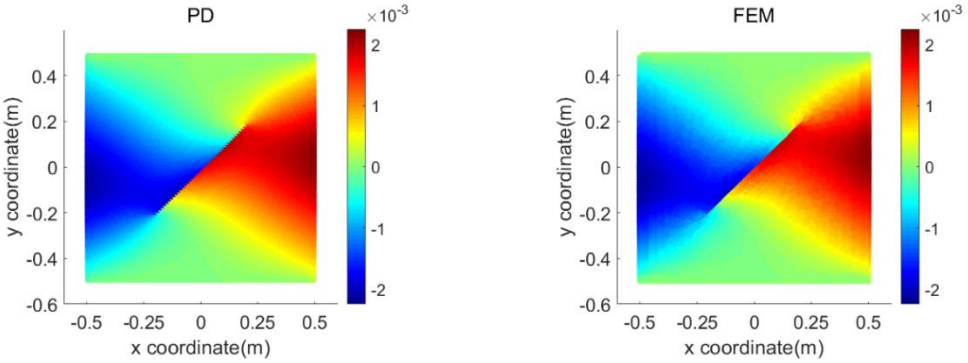

(a) The horizontal displacement field of the plate with initial crack inside

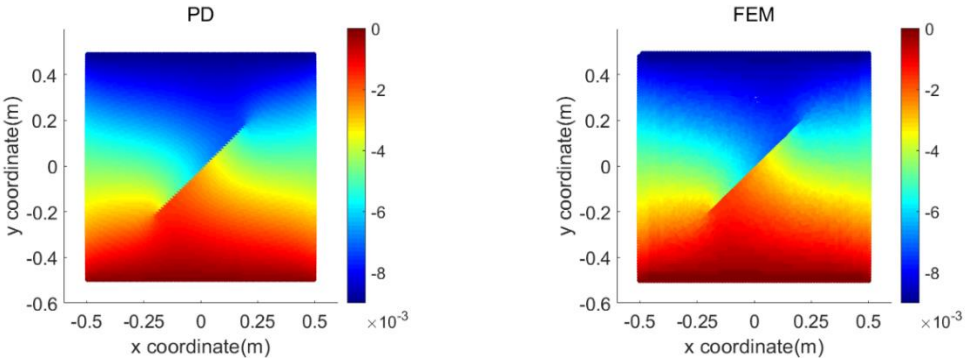

(b) The vertical displacement field of the plate with initial crack inside

Fig. 20 The comparison of the displacement field between PD and FEM without friction

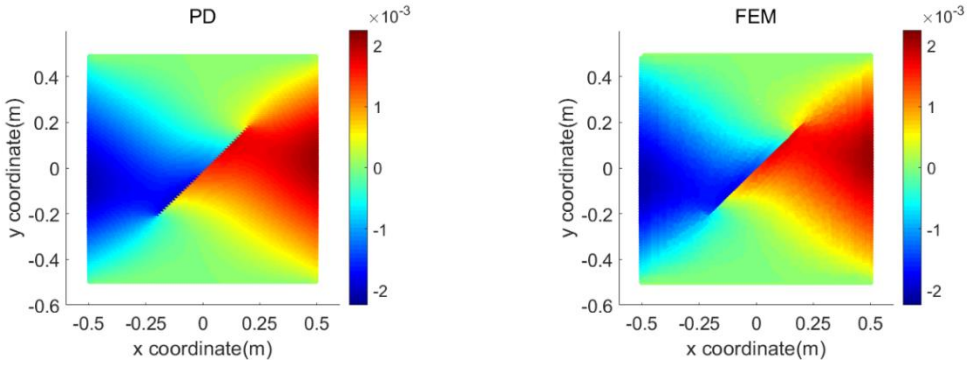

(a) The horizontal displacement field of the plate with initial crack inside

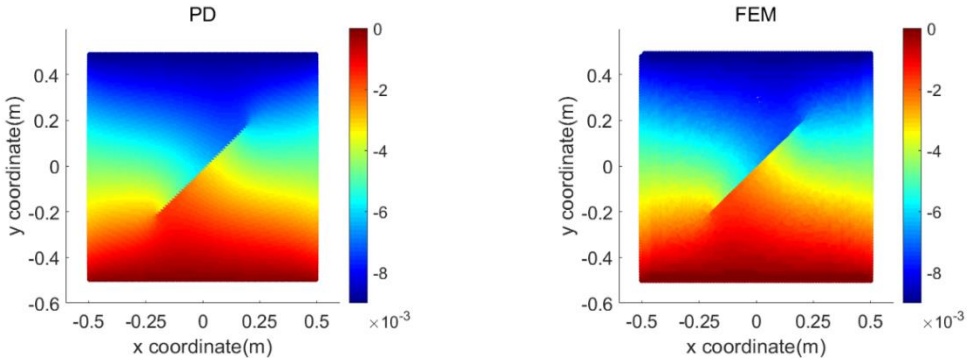

(b) The vertical displacement field of the plate with initial crack inside

Fig. 21 The comparison of the displacement field between PD and FEM (f_c = 0.8)

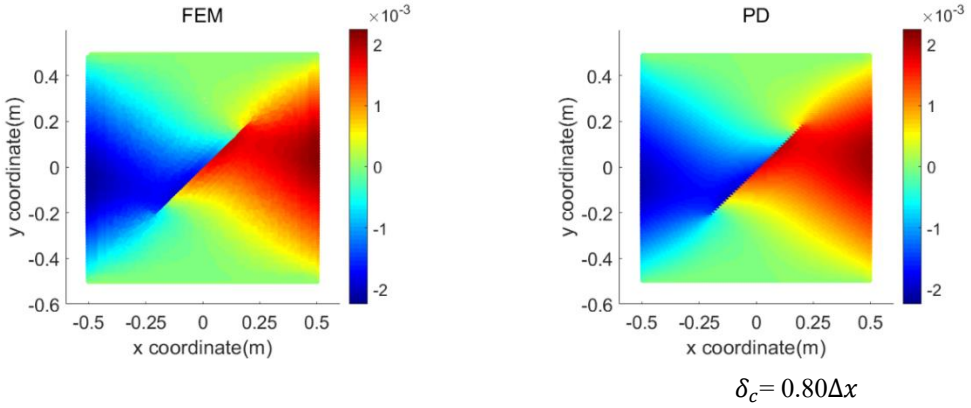

δ_c= 0.80Δx

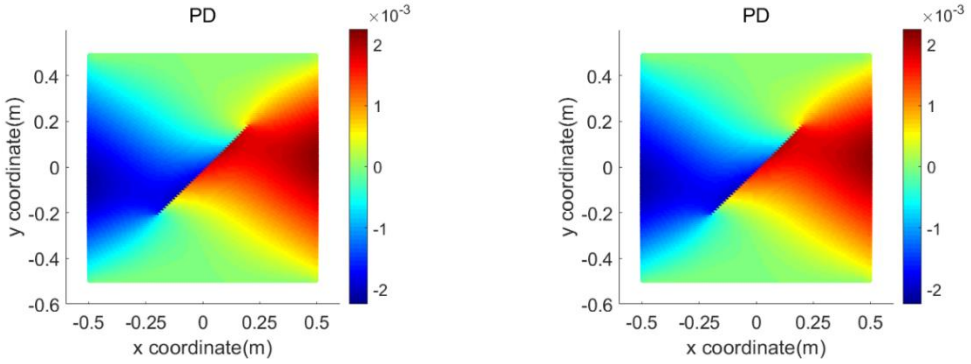

δ_c = 1.00Δx δ_c= 1.20Δx

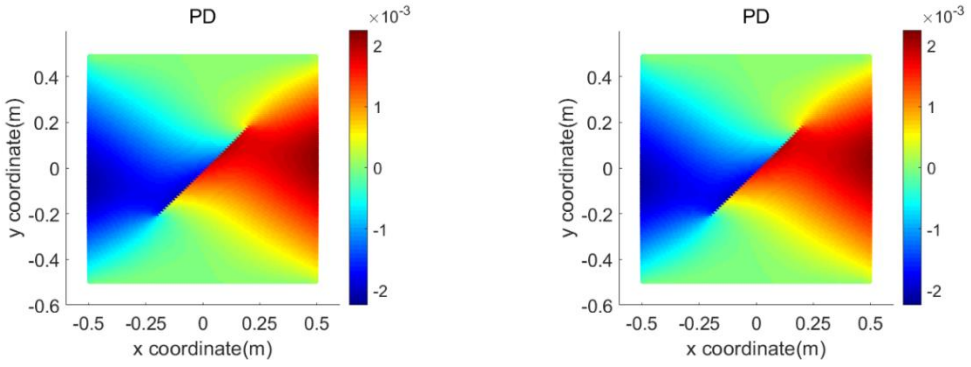

$\delta_c = 2.00\Delta x$ $\delta_c = 2.50\Delta x$

Fig. 22 The comparison of the horizontal displacement field with different contact radius

The effect of the contact radius on the fracture of plate is also investigated in this section. Figure 22 indicates the horizontal displacement of the plate without friction ($f_c = 0$). By changing the contact radius, the horizontal displacement shows small difference. In this case, the friction model is less sensitive to the critical contact radius.

4.4 The propagation of the frictional crack

In this section, the peridynamic contact model is considered to investigate the propagation of an initial crack. The geometry of the numerical case is depicted in Figure 23. The plate has a length of L=4.0m and a width of W=2.0m. An inclined pre-existing crack is included with 45 degrees to the x axis from coordinate (0,0.7) to (1.3,2.0) inside the plate. To insert the initial crack, the bonds passing through the connecting line between (0,0.7) and (1.3,2.0) need to be set as ruptured bonds. The plate behaves as a linear elastic material with the elastic modulus of E=10GPa and Poisson's ratio of v=0.3. A displacement with a constant increment of $\Delta d = 2.5 \times 10^{-3}$m at every time step is applied on the top boundary of the plate, with total 6 load steps during the simulation. Three fictious layers of material points are added at the top edge of the plate as the fictious region to transfer the external loading. The horizontal displacement of the particles in the fictious region is set to zero. The adaptive dynamic relaxation is used in each time step to guarantee the stability of the numerical algorithm. To constrain the plate, three virtual layers of material points are added at the bottom edge of the plate, setting the vertical displacement as zero. In order to constrain the right bottom corner of the plate, a 3×3 matrix of fictious particles is added by defining the displacement as zero. The solution domain is discretized into 100 and 200 material points along the horizontal and vertical directions, respectively. The radius of horizon is defined as $\delta = 6.0 \times 10^{-2}$m, i.e. three times of the distance between material points. The contact radius here is equal to Δx. The friction coefficient of the contact surface is set as 0.3.

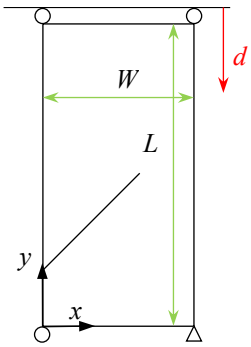

Fig. 23 The geometry sketch of the frictional crack propagation

Under the assumption of small deformations, when searching the corresponding contact points of a material point near the crack, the corresponding points can be regarded inside the horizon centered by this referred particle. Thus, the estimation of whether there is a contact force between two particles can be linked with the failure coefficient of the bond. When the bond is ruptured, the failure coefficient is equal to 0, which means if the distance between two material points is shorter than the contact radius in the current configuration, the contact interaction needs to be considered between this pair of particles. Otherwise, no contact force exists inside the pair of material points. To find out the fracture mode of the plate in this case, the stress intensity factor is calculated by ANSYS as

$$\mathrm{K_I} = 4.7262 \times 10^6 \mathrm{Pa} \cdot \sqrt{\mathrm{m}} \qquad \mathrm{K_{II}} = 2.6020 \times 10^7 \mathrm{Pa} \cdot \sqrt{\mathrm{m}} \tag{18}$$

The equation 18 shows clearly that the shear dominates the fracture. Therefore, the critical energy release rate G_c is regarded as mode II fracture energy here, defined as $G_c = 50\mathrm{KJ/m^2}$. Since, the critical stretch failure criterion is no longer useful for mode II fracture, a new failure criterion needs to be proposed. In this section, the critical skew (CSK) criterion [56] is utilized to estimate the rupture of bond. According to Zhang and Qiao [56], the critical skew γ_c can be expressed as,

$$\gamma_c = \sqrt{\frac{75G_c\pi}{64\mu\delta}} \tag{19}$$

To calculate the bond skew γ, which is regarded as the reason to generate the shear deformation, a concerned bond is supposed to be introduced [56]. As shown in Figure 24, a reference bond ξ_{R0} and a concerned bond ξ_{R1} are defined in the reference configuration, starting from the same point $\mathbf{x}_O$. After deformation, the reference bond ξ_{R0} and the concerned bond ξ_{R1} are denoted with ξ_{C0} and ξ_{C1} in the current configuration, respectively. Bond ξ_{C0} and ξ_{R0} can be linked with the rotation matrix **R**, as defined in equation 20 as

$$\xi_{C0} = \mathbf{R}\xi_{R0} \tag{20}$$

where **R** can be expressed as

$$\mathbf{R} = \begin{bmatrix} \cos\beta & -\sin\beta \\ \sin\beta & \cos\beta \end{bmatrix} \tag{21}$$

in which β is rotation angle of the reference bond.

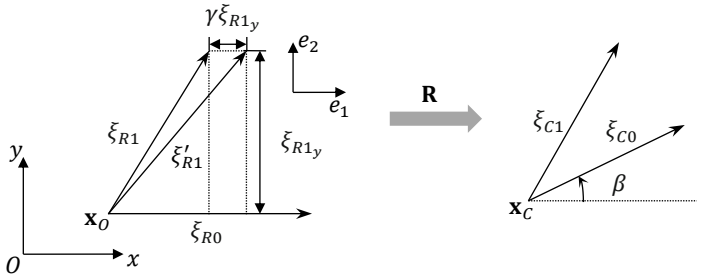

Fig. 24 The schematic to calculate bond skew

Under simple shear loading condition, the bond skew can be obtained from the deformation of the concerned bond ξ_{R1} relative to the reference bond ξ_{R0} as

$$\gamma = \left| \frac{(\xi'_{R1} - \xi_{R1}) \cdot e_1}{\xi_{R1} \cdot e_2} \right| \tag{22}$$

in which e_1 and e_2 are the unit vectors along the axis of local coordinate. Here, e_1 is defined parallel to the reference bond vector ξ_{R0}. ξ'_{R1} represents the current concerned bond in the reference configuration, starting with point $\mathbf{x}_O$, defined as

$$\xi'_{R1} = \mathbf{R}^T \xi_{C1} \tag{23}$$

In this case, the reference bond is defined along the direction of the crack. Thus, it can be regarded as unbroken bond and no updating of the reference bond is needed during the simulation.

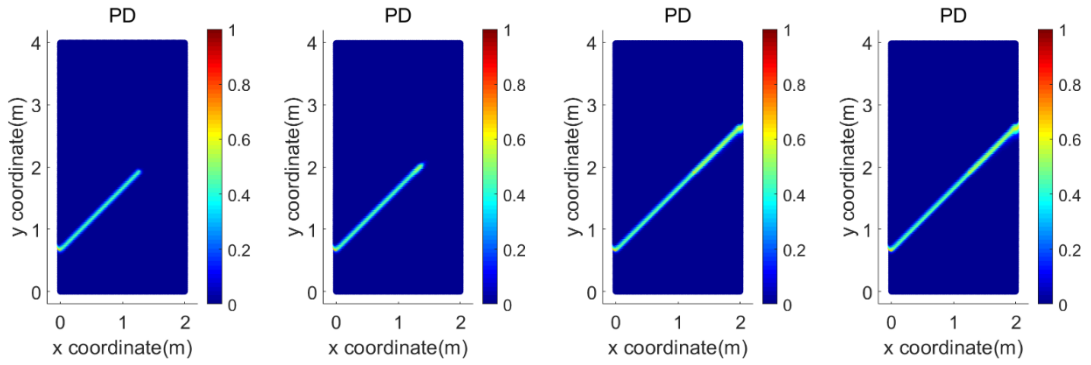

$d = 5.0\times 10^{-3}$m $d = 1.0\times 10^{-3}$m $d = 1.25\times 10^{-2}$m $d = 1.5\times 10^{-2}$m

Fig.25 The distribution of the local damage of the plate under different loading conditions

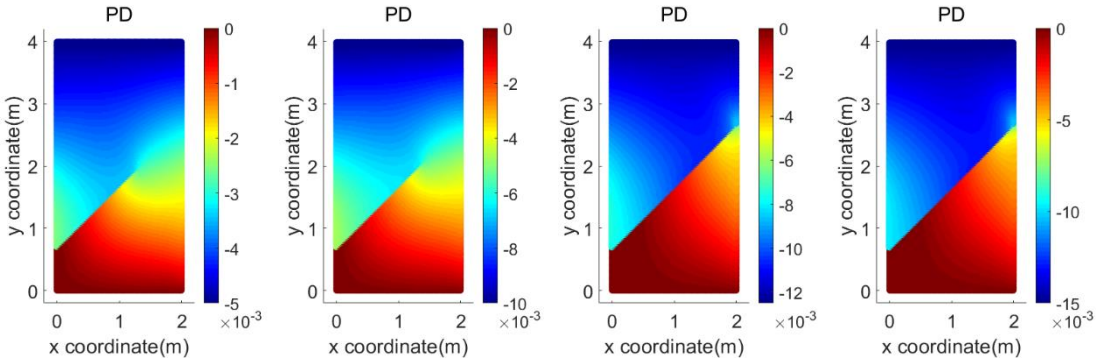

$d = 5.0\times 10^{-3}$m $d = 1.0\times 10^{-2}$m $d = 1.25\times 10^{-2}$m $d = 1.5\times 10^{-2}$m

Fig.26 The vertical displacement of the plate under different loading conditions

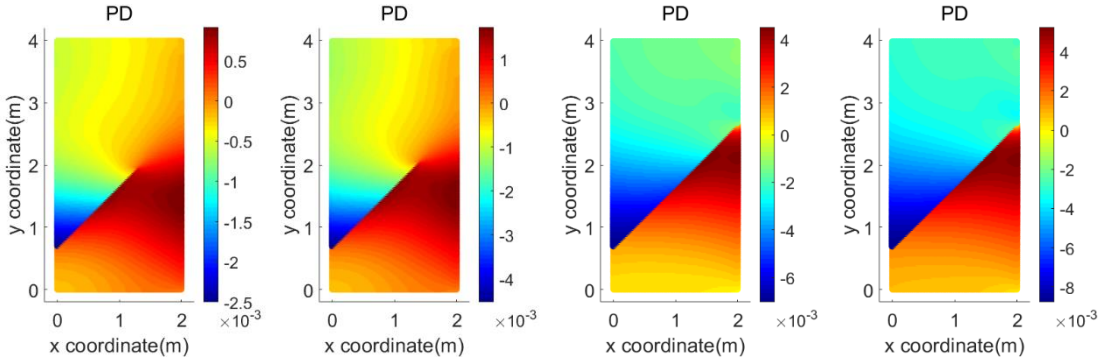

$d = 5.0\times 10^{-3}$m $d = 1.0\times 10^{-2}$m $d = 1.25\times 10^{-2}$m $d = 1.5\times 10^{-2}$m

Fig.27 The horizontal displacement of the plate under different loading conditions

Figure 25 indicates the propagation path of the frictional crack during the simulation. It can be seen clearly that when the loading displacement reached $d = 1.0\times 10^{-3}$m, the crack started to propagate. There was an obvious sliding along the crack. As the crack propagated, the sliding distance became more apparently, which can be seen in Figure 27. The crack grew along the direction of the crack. When the applied loading displacement is $d = 1.25\times 10^{-2}$m, the crack propagated through the whole plate, and the plate broke into two parts. It is clear to see the sliding on the tip angle of the plate. Then with the increase in the loading displacement, at the boundary of the plate, the growth path of the crack turned into a gentle curve. Peridynamic results are similar to the results given in [22] which were obtained by

using phase-field method.

5.Conclusion

In this paper, the propagation of frictional crack is modelled based on the ordinary state based peridynamics. A peridynamic contact model is introduced, in which the contact force is defined as a short-range force, occurred within a critical distance. Therefore, no other sophisticated algorithm is needed to impose the no-penetration constrains. In addition, compared with traditional numerical method like FEM, peridynamics has advantages dealing with the discontinuity issue, due to the integral form of the displacements in the equation of motion. In two-dimensional peridynamic contact model, the normal contact force is defined proportional to the deformation of the fictious bond along the normal direction, similar as idea of pairwise force in the bond based peridynamics. The friction force can be calculated with the Coulomb's law. By modelling the sliding of two plates and the plate with an initial crack under compression, the peridynamic contact model was validated. The contact model shows less sensitivity to the critical contact radius. Finally, based on the skew bond criterion, the propagation of the frictional crack is investigated. In conclusion, it was demonstrated that peridynamics can be an alternative option for modeling the frictional interfaces.

Acknowledgement

The authors gratefully acknowledge the support from Harbin Engineering University and the University of Strathclyde.

References

1. Li, X.F., Li, H.B. and Zhao, Y., 2017. 3D polycrystalline discrete element method (3PDEM) for simulation of crack initiation and propagation in granular rock. *Computers and Geotechnics* 90(10), pp.96-112.
2. Espinosa, H.D. and Zavattieri, P.D., 2003. A grain level model for the study of failure initiation and evolution in polycrystalline brittle materials. part II: numerical examples. *Mechanics of Materials*, 35(3/6), pp.365-394.
3. Ghajari, M., Iannucci, L. and Curtis, P., 2014. A peridynamic material model for the analysis of dynamic crack propagation in orthotropic media. *Computer Methods in Applied Mechanics and Engineering*, 276, pp.431-452.
4. Tan, Y., Yang, D. and Sheng, Y., 2009. Discrete element method (DEM) modeling of fracture and damage in the machining process of polycrystalline SiC. *Journal of the European Ceramic Society*, 29(6), pp.1029-1037.
5. Sfantos, G.K., and Aliabadi, M.H., 2010. A boundary cohesive grain element formulation for modelling intergranular microfracture in polycrystalline brittle materials. *International Journal for Numerical Methods in Engineering*, 69(8), pp.1590-1626.
6. Khoei, A.R., Biabanaki, S. and Parvaneh, S.M., 2013. 3D dynamic modeling of powder forming processes via a simple and efficient node-to-surface contact algorithm. *Applied Mathematical Modelling*, 37(1-2), pp.443–462.
7. Khoei, A.R., Biabanaki, S. and Parvaneh, S. M., 2012. Dynamic modeling of powder compaction processes via a simple contact algorithm. *International Journal of Mechanical Sciences*, 64(1), pp.196-210.

8. Wriggers, P., 1995. Finite element algorithms for contact problems. *Archives of Computational Methods in Engineering*, 2(4), pp.1-49.
9. Zhong, Z.H. and Mackerle, J., 1992. Static contact problems—a review. *Engineering Computations*, 9(1), pp.3-37.
10. Simo, J.C., Wriggers, P. and Taylor, R.L., 1985. A perturbed Lagrangian formulation for the finite element solution of contact problems. *Computer Methods in Applied Mechanics and Engineering*, 50(2), pp.163-180.
11. Chaudhary, A.B. and Bathe, K. J., 1986. A solution method for static and dynamic analysis of three-dimensional contact problems with friction. *Computers and Structures*, 24(6), pp.855-873.
12. Peri, D. and Owen, D., 1992. Computational model for 3D contact problems with friction based on the penalty method. *International Journal for Numerical Methods in Engineering*, 35(6), pp.1289-1309.
13. Mos, N., Dolbow, J. and Belytschko, T., 1999. A finite element method for crack growth without remeshing. *International Journal for Numerical Methods in Engineering*, 46(1), pp.131-150.
14. Belytschko, T. and Black, T., 1999. Elastic crack growth in finite elements with minimal remeshing. *International Journal for Numerical Methods in Engineering*, 45(5), pp.601-620.
15. Liu, F. and Borja, R. I., 2008. A contact algorithm for frictional crack propagation with the extended finite element method. *International Journal for Numerical Methods in Engineering,* 76(10), pp.1489-1512.
16. Dolbow, J., Moes, N. and Belytschko, T., 2001. An extended finite element method for modeling crack growth with frictional contact. *Computer Methods in Applied Mechanics and Engineering*, 190(51–52), pp.6825-6846.
17. Khoei, A.R. and Nikbakht, M., 2007. An enriched finite element algorithm for numerical computation of contact friction problems. *International Journal of Mechanical Sciences*, 49(2), pp. 183-199.
18. Ji, H. and Dolbow, J.E., 2004. On strategies for enforcing interfacial constraints and evaluating jump conditions with the extended finite element method. *International Journal for Numerical Methods in Engineering*, 61(14), pp.2508–2535.
19. Moës, N., Béchet, E. and Tourbier, M., 2010. Imposing Dirichlet boundary conditions in the extended finite element method. *International Journal for Numerical Methods in Engineering,* 67(12), pp.1641-1669.
20. Hirmand, M., Vahab, M. and Khoei, A.R., 2015. An augmented Lagrangian contact formulation for frictional discontinuities with the extended finite element method. *Finite Elements in Analysis and Design*, 107, pp.28-43.
21. Coon, E.T., Shaw, B.E. and Spiegelman, M., 2011. A nitsche-extended finite element method for earthquake rupture on complex fault systems. *Computer Methods in Applied Mechanics and Engineering*, 200(41-44), pp.2859-2870.
22. Fei, F. and Choo, J., 2020. A phase-field method for modeling cracks with frictional contact. *International Journal for Numerical Methods in Engineering*, 121, pp.740-762.
23. Silling S. A., 2000. Reformulation of elasticity theory for discontinuities and long-range forces. *Journal of the Mechanics and Physics of Solids,* 48(1), pp.175-209.
24. Imachi, M., Tanaka, S., Bui, T.Q., Oterkus, S. and Oterkus, E., 2019. A computational approach based on ordinary state-based peridynamics with new transition bond for dynamic fracture analysis. *Engineering Fracture Mechanics*, 206, pp.359-374.

25. De Meo, D. and Oterkus, E., 2017. Finite element implementation of a peridynamic pitting corrosion damage model. *Ocean Engineering*, 135, pp.76-83.
26. Diyaroglu, C., Oterkus, S., Oterkus, E. and Madenci, E., 2017. Peridynamic modeling of diffusion by using finite-element analysis. *IEEE Transactions on Components, Packaging and Manufacturing Technology*, 7(11), pp.1823-1831.
27. Zhu, N., De Meo, D. and Oterkus, E., 2016. Modelling of granular fracture in polycrystalline materials using ordinary state-based peridynamics. *Materials*, 9(12), p.977.
28. Basoglu, M.F., Zerin, Z., Kefal, A. and Oterkus, E., 2019. A computational model of peridynamic theory for deflecting behavior of crack propagation with micro-cracks. *Computational Materials Science*, 162, pp.33-46.
29. Diyaroglu, C., Oterkus, S., Oterkus, E., Madenci, E., Han, S. and Hwang, Y., 2017. Peridynamic wetness approach for moisture concentration analysis in electronic packages. *Microelectronics Reliability*, 70, pp.103-111.
30. Imachi, M., Tanaka, S., Ozdemir, M., Bui, T.Q., Oterkus, S. and Oterkus, E., 2020. Dynamic crack arrest analysis by ordinary state-based peridynamics. *International Journal of Fracture*, 221(2), pp.155-169.
31. Yang, Z., Vazic, B., Diyaroglu, C., Oterkus, E. and Oterkus, S., 2020. A Kirchhoff plate formulation in a state-based peridynamic framework. *Mathematics and Mechanics of Solids*, 25(3), pp.727-738.
32. Vazic, B., Wang, H., Diyaroglu, C., Oterkus, S. and Oterkus, E., 2017. Dynamic propagation of a macrocrack interacting with parallel small cracks. *AIMS Materials Science*, 4(1), pp.118-136.
33. Kefal, A., Sohouli, A., Oterkus, E., Yildiz, M. and Suleman, A., 2019. Topology optimization of cracked structures using peridynamics. *Continuum Mechanics and Thermodynamics*, 31(6), pp.1645-1672.
34. De Meo, D., Russo, L. and Oterkus, E., 2017. Modeling of the onset, propagation, and interaction of multiple cracks generated from corrosion pits by using peridynamics. *Journal of Engineering Materials and Technology*, 139(4).
35. Ozdemir, M., Kefal, A., Imachi, M., Tanaka, S. and Oterkus, E., 2020. Dynamic fracture analysis of functionally graded materials using ordinary state-based peridynamics. *Composite Structures*, 244, p.112296.
36. Huang, Y., Oterkus, S., Hou, H., Oterkus, E., Wei, Z. and Zhang, S., 2019. Peridynamic model for visco-hyperelastic material deformation in different strain rates. *Continuum Mechanics and Thermodynamics*, pp.1-35.
37. Vazic, B., Oterkus, E. and Oterkus, S., 2020. Peridynamic model for a Mindlin plate resting on a Winkler elastic foundation. *Journal of Peridynamics and Nonlocal Modeling*, pp.1-10.
38. Nguyen, C.T. and Oterkus, S., 2019. Peridynamics for the thermomechanical behavior of shell structures. *Engineering Fracture Mechanics*, 219, p.106623.
39. Nguyen, C.T. and Oterkus, S., 2019. Peridynamics formulation for beam structures to predict damage in offshore structures. *Ocean Engineering*, 173, pp.244-267.
40. Zhou, X., and Wang, Y., 2021. State-of-the-art review on the progressive failure characteristics of geomaterials in peridynamic theory. *Journal of Engineering Mechanics*, 147(1), 03120001.
41. Wang, Y., Zhou, X. and Xu, X., 2016. Numerical simulation of propagation and coalescence of flaws in rock materials under compressive loads using the extended non-ordinary state-based peridynamics. *Engineering Fracture Mechanics*, 163, pp.248-273.
42. Zhou, X., and Wang, Y., 2016. Numerical simulation of crack propagation and coalescence in pre-

cracked rock-like brazilian disks using the non-ordinary state-based peridynamics. International *Journal of Rock Mechanics and Mining Sciences*, 89, pp.235-249.

43. Wang, Y., Zhou, X., Wang, Y., and Shou, Y., 2018. A 3-D conjugated bond-pair-based peridynamic formulation for initiation and propagation of cracks in brittle solids. *International Journal of Solids and Structures*, 134, pp.89-115.
44. Wang, Y., Zhou, X., and Shou, Y., 2017. The modeling of crack propagation and coalescence in rocks under uniaxial compression using the novel conjugated bond-based peridynamics. *International Journal of Mechanical Sciences*, 128, pp.614-643.
45. Wang, Y., Zhou, X., and Kou, M., 2019. Three-dimensional numerical study on the failure characteristics of intermittent fissures under compressive-shear loads. *Acta Geotechnica*, 14 (4), pp.1161-1193.
46. Zhou, X., Wang, Y., and Shou, Y., 2020. Hydromechanical bond-based peridynamic model for pressurized and fluid-driven fracturing processes in fissured porous rocks. *International Journal of Rock Mechanics and Mining Sciences*, 132, 104383.
47. Kamensky, D., Behzadinasab, M., Foster, J.T. and Bazilevs, Y., 2019. Peridynamic modeling of frictional contact. *Journal of Peridynamics and Nonlocal Modeling,* 1, pp.107-121.
48. Zhang, Y. and Qiao, P., 2019. Peridynamic simulation of two-dimensional axisymmetric pull-out tests. *International Journal of Solids and Structures*, 168, pp.41-57.
49. Silling, S.A., Epton, M., Weckner, O., Xu, J. and Askari, E., 2007. Peridynamic states and constitutive modeling. *Journal of Elasticity*, 88(2), pp.151-184.
50. Le, Q.V., Chan, W.K. and Schwartz, J., 2014. A two-dimensional ordinary, state-based peridynamic model for linearly elastic solids. *International Journal for Numerical Methods in Engineering*, 98(8), pp.547-561.
51. Silling, S.A. and Lehoucq, R.B., 2010. Peridynamic theory of solid mechanics. *Advances in Applied Mechanics*, 44(10), pp.73-168.
52. Madenci, E. and Oterkus, E., 2014. *Peridynamic theory and its applications*. New York: Springer.
53. Bi, J. and Zhou, X., 2017. Numerical simulation of kinetic friction in the fracture process of rocks in the framework of general particle dynamics. *Computers and Geotechnics*, 83, pp.1-15.
54. Dipasquale, D., Sarego, G., Zaccariotto, M. and Galvanetto, U., 2017. A discussion on failure criteria for ordinary state-based peridynamics. *Engineering Fracture Mechanics*, 186, pp.378-398.
55. Popov, V.L., 2010. *Contact Mechanics and Friction*. Berlin Heidelberg, Springer.
56. Zhang, Y., and Qiao, P., 2019. A new bond failure criterion for ordinary state-based peridynamic mode ii fracture analysis. *International Journal of Fracture*, 215, pp.105-128.